Journal of Materials Research and Technology 42 (2026) 3057–3071

Contents lists available at ScienceDirect

Journal of Materials Research and Technology

journal homepage: www.elsevier.com/locate/jmrt

# Direct aging of AlSi10Mg alloy produced by powder bed fusion – laser beam: Eliminating the need for solution heat treatment

R.L. Batalha [a,b,c,*], C.M. Ferreira [b,d,e,**], A.C. Silva [f], L. Reis [d,e], R. Cláudio [b,e,g], M.J. Carmezim [b,h], P. Ramasamy [i,j], L.B. Godefroid [k,l], S.C. de Araújo [l], G.L. de Faria [k,l], P.J. Morais [a]

[a] Instituto de Soldadura e Qualidade (ISQ), Av. Prof. Dr. Cavaco Silva, Porto Salvo, 2740-120, Portugal
[b] Escola Superior de Tecnologia de Setúbal, Polytechnic Institute of Setúbal, 2910-761, Setúbal, Portugal
[c] ENIDH – Escola Náutica Infante D. Henrique, 2770-058, Paço de Arcos, Portugal
[d] Instituto Superior Técnico, University of Lisbon, Av. Rovisco Pais, 1049-001, Lisboa, Portugal
[e] IDMEC, Instituto Superior Técnico, University of Lisbon, Av. Rovisco Pais, 1049-001, Lisboa, Portugal
[f] Department of Materials Science, NOVA School of Science and Technology, NOVA University Lisbon, 2829-516, Caparica, Portugal
[g] DICE Lab, Polytechnic Institute of Setúbal, 2910-761, Setúbal, Portugal
[h] CQE, IMS, Instituto Superior Técnico, University of Lisbon, Av. Rovisco Pais, 1049-001, Lisboa, Portugal
[i] Erich Schmid Institute of Materials Science of the Austrian Academy of Sciences, Jahnstraße 12, Leoben, 8700, Austria
[j] Chair of Materials Physics, Montanuniversität Leoben, Franz-Josef-Straße 18, Leoben, 8700, Austria
[k] Department of Metallurgical and Materials Engineering, School of Mines, Federal University of Ouro Preto, 35400-000, Ouro Preto, Minas Gerais, Brazil
[l] REDEMAT – Graduate Program on Materials Engineering, School of Mines, Federal University of Ouro Preto, 35400-000, Ouro Preto, Minas Gerais, Brazil

ARTICLE INFO

*Keywords:*
Additive manufacturing
Powder bed fusion
Al–Si alloys
Heat treatment
Aging curves
Precipitation kinetics

ABSTRACT

The AlSi10Mg alloy is widely used in metal additive manufacturing (AM), yet optimal post-processing routes for components produced by Powder Bed Fusion-Laser Beam (PBF-LB/M) remain unclear due to their highly refined and non-equilibrium microstructures. Conventional T6 heat treatments, effective for cast alloys, often cause softening in PBF-LB/M AlSi10Mg. This work establishes aging curves through a systematic assessment of temperature-time combinations and correlates them with microstructural evolution and mechanical behavior. The as-built alloy exhibited a supersaturated and highly refined non-equilibrium microstructure, resulting in high tensile strength. Among all evaluated conditions, direct aging at 150 °C for 2 h (DA 150/2.0) produced the highest hardness and tensile performance without prior solution treatment. Natural aging for at least 48h was required to achieve peak hardness. DA 150/2.0 preserved the eutectic Si network while promoting dense precipitation of nanometric Si particles, which improved strengthening via the Orowan mechanism. This condition increased yield and ultimate tensile strengths by 17% and 13%, respectively, and enhanced ductility relative to the as-built state. Higher-temperature treatments dissolved the cellular structure and coarsened Si, reducing strength. Overall, this study demonstrates that low-temperature direct aging offers an efficient route to optimize the strength-ductility balance of PBF-LB/M AlSi10Mg without solution treatment.

## 1. Introduction

Additive manufacturing (AM) enables the production of near-net shape parts, expanding the design space of engineering components because of a layer-wise fabrication built from a digital model [1]. AM has seen increased adoption as a driver of the ongoing digital transformation in the manufacturing industry. The major advantage of AM is a streamlined product life cycle from design to production of final parts, leading to accelerated time-to-market [2].

Aluminum alloys and AM have been an important combination in the advanced manufacturing of lightweight and complex shape parts in the aerospace and automotive industries [3]. This technology has already been adopted for flight-qualified satellite hardware (e.g., topologically optimized antenna brackets for Sentinel satellites), aeronautical

* Corresponding author. Instituto de Soldadura e Qualidade (ISQ), Av. Prof. Dr. Cavaco Silva, Porto Salvo, 2740-120, Portugal.
** Corresponding author. Escola Superior de Tecnologia de Setúbal, Polytechnic Institute of Setúbal, 2910-761, Setúbal, Portugal.
*E-mail addresses:* rlbatalha@isq.pt (R.L. Batalha), carla.m.ferreira@estsetubal.ips.pt (C.M. Ferreira).

https://doi.org/10.1016/j.jmrt.2026.03.256
Received 19 February 2026; Received in revised form 25 March 2026; Accepted 27 March 2026
Available online 28 March 2026

structural brackets, full-scale bicycle frame, and compact crossflow minichannel heat exchangers [4–6]. The AlSi10Mg alloy has emerged as a reference material for AM [7]. It is a well-known hypoeutectic Al–Si alloy that can be age-hardened and has been used in conventional casting for a variety of engineering applications [3,7–9].

Powder Bed Fusion – Laser Beam (PBF-LB/M), currently the most used metal AM technology, applies a focused laser beam to melt a powder bed. The process induces an intrinsic thermal history, resulting in a remarkable metastable microstructure with refined cellular solidification structures due to high thermal gradients and cooling rates [1–3,7–9]. Although PBF-LB/M facilitates the manufacture of near-net-shape components with intricate geometry, the resulting microstructure and mechanical properties differ significantly from those of castings due to the multiple layer re-heating and considerably higher cooling rates involved ($10^3$–$10^7$ K/s) [7–10].

The fast solidification of Al–Si alloys produced by PBF-LB/M lead to solute trapping in the Al-matrix, with studies reporting 6–8 wt.% of Si in solid solution in the as-built condition [8,11], despite the maximum equilibrium solubility of 1.6 wt% Si in Al according to the Al–Si phase diagram [8–11]. Thus, the microstructure of heat-treatable alloys such as AlSi10Mg produced by PBF-LB/M is complex, heterogeneous, and hierarchical [11–13].

It has been shown that the highly refined solidification structure of α-Al cells surrounded by a Si network is the main reason for the high strength of AlSi10Mg alloys produced by PBF-LB/M [8,12–14]. AlSi10Mg parts produced by PBF-LB/M exhibit yield and ultimate tensile strengths exceeding 250 MPa and 450 MPa, respectively, which are significantly higher than the 170 MPa and 300 MPa reported for cast counterparts [8,9,12,14,15]. In addition, fine Si and $Mg_2Si$ precipitates have been identified within the Al matrix of as-built AlSi10Mg [8,11,16], together with a high dislocation density [13,17–20]. These microstructural features contribute to significant hardening through solid-solution, grain boundary (Hall-Petch effect), and Orowan strengthening mechanisms, leading to the observed high mechanical strength and hardness of the Al–Si alloys processed by PBF-LB/M [17,20]. On the other hand, AlSi10Mg alloys produced by PBF-LB/M typically exhibit limited ductility, with total elongation commonly below 5% [12,14,21,22]. This reduced ductility is generally attributed to the presence of a continuous and brittle Si network along cell boundaries, pronounced microstructural heterogeneity, and process-induced porosity that promotes early crack initiation [12,21]. As a result, the mechanical performance of as-built AlSi10Mg is strongly strength-dominated and characterized by poor ductility, highlighting the importance of post-processing heat treatments to tailor the microstructure and achieve an improved strength-ductility balance.

Heat treatment is a key post-processing stage for PBF-LB/M alloys, as it allows the adjustment of material performance to meet application-specific requirements [23,24]. It has been shown that post-processing strongly influences the mechanical properties of AlSi10Mg, with ductility ranging from 5.6 to 38.8% and tensile strength from 184 to 479 MPa [8,9,14,23]. Stress relieving (SR) at 200–300 °C for 1–2 h is generally adopted to reduce residual stresses in AlSi10Mg following PBF-LB/M [8,13,24]. A significant loss in mechanical strength with a corresponding increase in ductility has been reported after SR, since it induces not only dislocation annihilation and recovery, but it also coarsens the microstructure through diffusion-based processes [8,12,13]. Zhao et al. (2019) observed that SR at 250 °C resulted in a thicker Al–Si eutectic network surrounding the α-Al cells and the formation of larger, more acicular Si-rich precipitates compared with the as-built state [12]. When the SR was performed at 300 °C, the Al/Si eutectic transformed into globular Si particles [12]. Similarly, Cauwenbergh et al. (2021) reported spheroidization of the Al–Si eutectic microstructure after SR at 270 °C [8]. As a result of reduced Si supersaturation in α-Al and coarsening of the eutectic microstructure, SR generally results in reduced strength and improved ductility in AlSi10Mg parts [8,12,13].

Heating the build plate is another commonly used method to reduce residual stress evolved during PBF-LB/M [16,21,25]. However, this approach introduces uncertainty in the materials behavior since it is not possible to ensure that the part is uniformly heated. Platform temperatures between 80 and 200 °C are normally applied when processing AlSi10Mg to mitigate residual stress and minimize distortions [25,26]. Nonetheless, elevated substrate temperature may cause microstructural gradients along the build height, as it can induce *in-situ* aging of the alloy exposed to a relatively high temperature during the process, leading to coarsening of the as-built microstructure [25,26].

Altering the mechanical properties of materials produced by PBF-LB/M through heat treatment is often done using procedures originally developed for conventionally manufactured alloys, without considering the distinct microstructures obtained in PBF-LB/M. As reported by Kumar et al. (2025) and Amith et al. (2025), the application of the standardized T6 temper to the AlSi10Mg alloy fabricated by AM results in materials softening, which is the opposite to the intended strengthening effect [27,28]. These findings raise concerns about the suitability of traditional heat treatments for PBF-LB/M materials. Moreover, Merino et al. (2021) performed a comprehensive study on several heat treatments applied to PBF-LB/M AlSi10Mg, including stress relief (SR), hot-isostatic pressing (HIP) and T6, followed by aging. According to them, aging can allow systematic changes in both strength and ductility [9]. Therefore, although the T6 and annealing treatments are appropriate for cast Al alloys, they are not optimal for the fine microstructure of PBF-LB/M alloys.

Alternatively, several authors have investigated direct aging (DA) as a more effective approach to strengthening the AlSi10Mg alloy produced by PBF-LB/M without the solution step normally performed in the T6 temper, hence inducing aging directly to the as-manufactured material [19,29–32]. The absence of the initial high-temperature solution treatment may offer considerable advantages, as it preserves the as-built Si morphology while still enabling controlled precipitation from the supersaturated α-Al matrix resulting from the PBF-LB/M process. Nonetheless, DA has been shown to have complex effects on the non-equilibrium microstructure of AlSi10Mg produced by PBF-LB/M. Zhang et al. (2023) studied DA at 170 °C for 4 h and 24 h and reported that it induced precipitation of nanometric Si particles in the α-Al matrix while retaining the refined microstructure, thus ensuring high strength [30]. When the DA was extended to 24 h, the precipitates were coarsened accompanied by a decrease in their volume fraction [30]. Similarly, Zhang et al. (2022) observed significant microstructural changes after aging at 130 °C and 190 °C for 4 h, with corresponding effects on mechanical properties. Low-temperature aging at 130 °C improved both tensile strength and ductility, and the authors emphasized that optimized DA may enhance mechanical properties [21]. Casati et al. (2018) reported that, after direct aging at 160 °C, the AlSi10Mg showed a strength of 493 MPa and elongation of 6% along the building direction [26]. Baek et al. (2021) pointed out that direct aging not only improved the performance, but also significantly improved the fatigue properties of AlSi10Mg [33]. It is well established that fatigue performance, particularly in the high-cycle regime, is closely related to tensile strength [33]. Accordingly, direct aging (DA) treatments are expected to promote significant improvements in the high-cycle fatigue behavior of PBF-LB/M AlSi10Mg. This expectation is consistent with a previous study [34], which reports markedly superior fatigue performance after DA when compared with both as-built and conventionally T6-treated conditions.

Based on previous studies, typical heat treatments for the AlSi10Mg alloy include direct aging (130–250 °C), stress relieving (250–320 °C), and solution heat treatment (400–540 °C). These post-processing routes generally lead to the following decreasing strength response in AlSi10Mg produced by PBF-LB/M: direct aging (DA), as-built, stress relieving (SR), HIP + aging, solution heat treatment (SHT) + aging (T6), HIP, and SHT [8,9,14]. Although most publications report optimal PBF-LB/M process parameters, deviations from nominal conditions can still occur and generate locally distinct thermal histories, even when

process parameters remain constant. This is particularly relevant for complex geometries, which can promote microstructural and defect variability due to non-uniform heat flow during fabrication. Therefore, a comprehensive understanding of post-processing heat treatment is essential to establish the process–structure–property relationships that govern the mechanical performance of the AlSi10Mg alloy produced by PBF-LB/M.

Although several studies have explored direct aging (DA) as an alternative to the conventional T6 temper for PBF-LB/M AlSi10Mg, no clear consensus has yet been reached regarding the temperature-time conditions required to achieve peak aging. Most published works focus on isolated aging conditions, often restricted to a single temperature and a limited time interval, which leaves the overall aging response of the alloy insufficiently understood. Moreover, the complex non-equilibrium microstructure generated by PBF-LB/M introduces additional challenges, making established heat-treatment practices for traditional cast Al–Si alloys poorly transferable. To address these knowledge gaps, the present work provides a systematic construction of aging curves for PBF-LB/M AlSi10Mg over a relatively wide range of temperature-time combinations, followed by a detailed correlational analysis linking microstructural evolution, Si-precipitation evolution, and mechanical performance. Particular attention is dedicated to evaluating whether a combination of high strength and improved ductility can be achieved directly from aging the as-manufactured condition, without the need for a prior solution treatment.

## 2. Materials and methods

### 2.1. Material and specimens preparation

Samples of the AlSi10Mg alloy were produced by powder bed fusion-laser beam (PBF-LB/M) in a Renishaw RenAM 500S Flex system with a 500 W ytterbium fiber laser ($\lambda = 1080$ nm), spot size of 80 μm, and continuous laser mode. The following commercial process parameters were used: laser power 500 W, scanning speed 2500 mm/s, hatching distance 0.09 mm, layer thickness 0.06 mm, and meander scanning strategy with 67° rotation between layers, as provided by Renishaw plc. A reduced build volume ($78 \times 78 \times 50$ mm$^3$) setup was used in the present work since it requires significantly less material. Hence, all samples were produced on AA5083 build plates (W: 78 mm, L: 78 mm, t: 9 mm) at room temperature, with laser focus position $F = 0$ mm, and continuous high purity Ar (99.999%) flow (190 m$^3$/h) for chamber inertization. The print job was set to start only when the chamber atmosphere reached a maximum oxygen content of 500 ppm. The raw material used was fresh commercial prealloyed AlSi10Mg spherical powder (Fig. 1a) with the following nominal chemical composition (wt. %): Al–10Si-0.35Mg-0.25Fe-0.1Mn-0.1Zn-0.05Cu (Renishaw plc).

Cuboid specimens (L: 18 mm, W: 8 mm, H: 8 mm) were first fabricated to establish the aging curves. In addition, cylindrical specimens (ϕ13 × 49 mm, Fig. 1b) were printed with orientations parallel to the building direction (BD or vertical, V) and the scanning direction (SD or horizontal, H). These specimens were subsequently heat-treated according to conditions selected from the aging curves and then machined for tensile tests.

### 2.2. Heat treatments

Aging curves were built by applying direct aging (DA) to cuboids of the AlSi10Mg alloy, varying the temperature from 100 to 300 °C (step of 50 °C) and time from 0.5 to 4.0 h (interval of 0.5 h), followed by Vickers macrohardness measurements. Moreover, solution and T6 treatments were also performed to the alloy. The standardized solution treatment (ST) and T6 temper (denoted ST ASTM and T6 ASTM) were performed in accordance with ASTM F3301-18a [35]. The alternative ST and T6 treatments (denoted as ST ISQ and T6 ISQ) correspond to modified heat-treatment conditions adapted from previous studies [15,36], in which the solution treatment and aging times were significantly reduced. The investigated conditions are summarized in Table 1.

The solution treatments were performed in a Nabertherm NW 200 furnace with the samples inside a protective gas-box and continuous high purity Ar flow (20 L/min), with a heating rate of 8 °C/min, followed by quenching in still water at room temperature. The aging step for the T6 tempers and direct aging treatments was carried out in a Thermo Scientific VT 6060 oven under vacuum ($10^{-4}$ mbar), using the oven's intrinsic heating profile, corresponding to an average heating rate of approximately 3 °C/min.

### 2.3. Simulation of precipitation-strengthening kinetics

A physically based numerical framework, implemented as a Python algorithm, was developed to simulate the precipitation kinetics and corresponding hardness evolution of the studied Al–Si–Mg alloy subjected to direct aging and T6 conditions. The model couples the nucleation, growth, and transformation of $Mg_2Si$-related phases with the

**Table 1**
Investigated conditions.

| Condition | Solubilizing | Quenching | Age hardening |
|---|---|---|---|
| AB | - | - | - |
| DA | - | - | 100–300 °C; 0.5–4.0h; air cooling |
| ST ASTM | 530°C; 6h | Water at RT | - |
| T6 ASTM | 530°C; 6h | Water at RT | 160°C; 6h; air cooling |
| ST ISQ | 530 °C; 1h | Water at RT | - |
| T6 ISQ | 530 °C; 1h | Water at RT | 170 °C; 2h; air cooling |

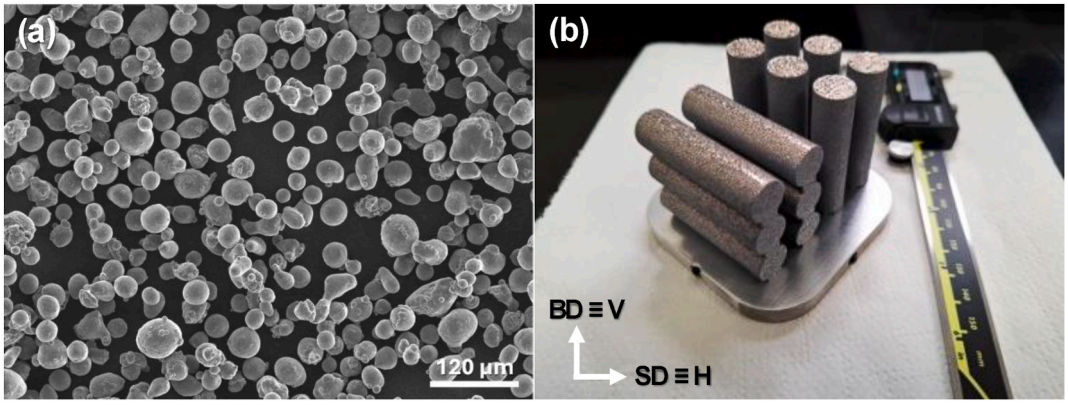


**Fig. 1.** (a) AlSi10Mg prealloyed powder ($d_{10} = 28$ μm; $d_{50} = 41$ μm; $d_{90} = 62$ μm) used as raw material and (b) as-built cylinders (ϕ13 × 49 mm). H denotes the horizontal direction (parallel to the scanning direction, SD), and V denotes the vertical direction (parallel to the building direction, BD).

coarsening of primary Si particles and incorporates a precipitation-strengthening law combining cutting and Orowan mechanisms. The modeling framework follows established methods reported in the literature [37–40] and was adapted to the present alloy system and heat-treatment conditions. The algorithm integrates classical nucleation theory, diffusion-controlled growth, and a Lifshitz–Slyozov–Wagner (LSW) coarsening module. In the developed algorithm, conditions DA and T6 are distinguished not only by the aging temperature as in previous models but, above all, by the representation of the initial microstructure, a decisive factor in accurately reproducing the physical behavior of these heat treatment routes. A detailed description of the kinetic models, including governing equations and input parameters, is provided in the Supplementary Information.

### 2.4. Microstructural characterization

The chemical composition of bulk samples of the AlSi10Mg alloy (Table 2) was obtained by spark emission spectroscopy using the OBLF QSN 750II spectrometer (Gesellschaft für Elektronik und Feinwerktechnik GmbH), and it was noticed that the chemical composition was not changed after heat treatment.

Then, structural analysis was performed by powder X-ray diffraction in a Rigaku MiniFlex diffractometer, using a Cu $k_\alpha$ ($\lambda = 1.5406$ Å) radiation operated at 30 kV and 15 mA in Bragg-Brentano geometry. The scan range was 20-90° with a step size of 0.02° and a scan speed of 0.5°/min. A full-pattern Rietveld refinement was performed for quantification using MAUD v2.9999 [41,42]. The instrumental profile function was calibrated with a NIST Si powder standard. The fitting was performed using the pseudo-Voigt with Popa size-strain model and harmonic texture with fiber sample asymmetry model for all conditions [43]. Due to resolution limitations, the lattice strains were estimated from full-width half maximum (FWHM) measurements. The refinement was considered statistically valid after achieving a Weighted Profile R-factor, Rwp <10%. The calculated patterns are shown in Supplementary Fig. 2.

The microstructural characterization was performed on cuboid and cylindrical samples cut with orientations parallel to the building direction (vertical) and scanning direction (horizontal). The microstructure was investigated in cold-mounted metallographic samples prepared with a final polishing step in silica colloidal (0.06 μm), followed by etching with Keller.

The micrographs were obtained in a Nikon Eclipse LV150 N optical microscope (OM) with an integrated Imaging Source 5 MP digital camera. Furthermore, the sample microstructures were characterized in a Hitachi SU3900 scanning electron microscope (SEM), using secondary electrons (SE), back-scattered electrons (BSE), and energy-dispersive spectroscopy (EDS, Bruker XFlash 730 M) detectors. The microstructural quantifications were carried out in optical micrographs and SEM images using the Nikon NIS-Elements BR v.6.10.01 software. Porosity was quantified by image analysis of six optical micrographs acquired at 50× magnification from cuboid polished samples for each investigated condition (Supplementary Fig. 3). In addition, Si particle size and area fraction were evaluated from SEM images acquired within the melt pool (MP) and heat-affected zone (HAZ) regions at magnifications of 2000×, 5000x, and 10000x (Supplementary Fig. 4). Quantitative measurements of porosity, Si particle size, and Si area fraction were performed using digital image thresholding and pixel-based analysis implemented in Nikon NIS-Elements BR software (v.6.10.01).

**Table 2**
Chemical composition (wt.%) of as-built (AB), direct aged (DA) and T6 samples.

| Condition | Al | Si | Mg | Fe | Mn, Zn, Cu |
|---|---|---|---|---|---|
| AB | balance | 10.5 ± 0.02 | 0.39 ± 0.001 | 0.13 ± 0.001 | <0.005 |
| DA 150/2.0 | balance | 10.4 ± 0.05 | 0.39 ± 0.001 | 0.16 ± 0.002 | <0.005 |
| T6 ASTM | balance | 10.4 ± 0.12 | 0.35 ± 0.005 | 0.13 ± 0.003 | <0.005 |
| T6 ISQ | balance | 10.6 ± 0.06 | 0.36 ± 0.003 | 0.13 ± 0.001 | <0.005 |

### 2.5. Mechanical tests

The aging curves (Fig. 2) were obtained by measuring the Vickers macrohardness of the samples using an EMCO-TEST DuraScan G5 universal hardness tester (EMCO-TEST Prüfmaschinen GmbH). Measurements were performed with an applied load of 10 kgf for 15 s (HV10) in accordance with the ASTM E92-23 [44], and at least twelve indentations were made on polished samples. The effect of natural aging was examined by allowing the as-built samples to rest at room temperature for 24, 48, and 144 h before direct aging at 150 °C/2.0 h (inset of Fig. 2).

Tensile tests were carried out on specimens (gauge length: 20 mm; diameter: 4 mm) machined from cylindrical samples built in both the horizontal and vertical directions (Fig. 1b and Supplementary Figure S2.1), following the ASTM E8/8M − 2022 [45]. The tests were performed in an Instron 5566 electromechanical universal testing machine equipped with a 10 kN load-cell, applying a strain rate of $1 \times 10^{-4}$ $s^{-1}$. A contact extensometer was used to record the elongation. At least three specimens were tested for each condition. The yield strength ($\sigma_{YS}$) was obtained using the 0.2% offset method, while the elastic modulus (E), ultimate tensile strength $\sigma_{UTS}$, and total elongation ($\varepsilon_T$) were obtained from the engineering stress–strain curves. In the DA 150/2.0 condition, specimens were naturally aged for 48 h followed by direct aging at 150 °C/2.0 h before machining and tensile testing. The fractured tensile specimens were examined using the Hitachi SU3900 SEM with the SE detector.

## 3. Results

### 3.1. Aging curves

The aging curves are presented in Fig. 2. The AlSi10Mg alloy in the as-built (AB) condition exhibited a hardness of 124 HV10, which was considerably higher than that of the A360.0 AlSiMg die-cast alloy (61 HV10) and cast + T6 condition (102 HV10) specified in ASTM B85/B85M − 18 [46]. Furthermore, neither the T6 ASTM (90 HV10) nor the T6 ISQ (102 HV10) treatments hardened the alloy produced by PBF-LB/M. On the other hand, direct aging (DA) led to peak hardness in a very specific temperature–time combination: hardness increased with shorter aging time at 150 °C, reaching a peak value of (133 ± 2) HV10 at 150 °C/2.0 h (DA 150/2.0). Extending the time at 150 °C beyond 2 h did not further change the hardness.

It is important to note that the peak hardness of the DA 150/2.0

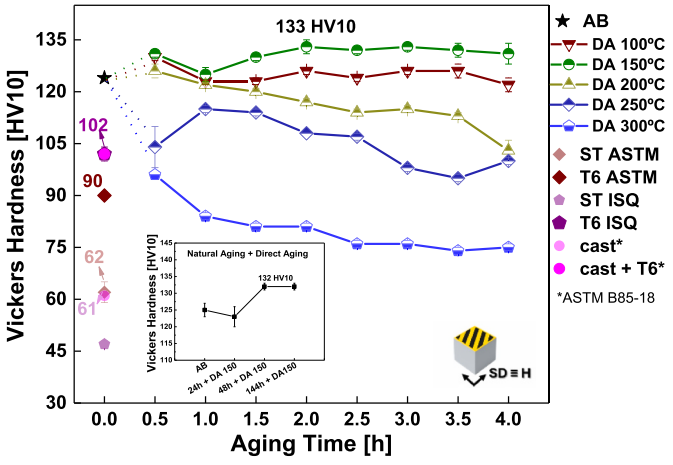


**Fig. 2.** Aging curves of the AlSi10Mg alloy produced by PBF-LB/M.

condition was measured after 48 h of natural aging, after which stabilization was observed (see inset of Fig. 2). The influence of natural aging was not systematically evaluated for the remaining temperature–time combinations, as the primary objective of this work was to establish the artificial aging response and identify the optimal processing window.

The hardness decreases sharply when the aging temperature increases: Direct aging at 200, 250, and 300 °C, which is frequently referred as stress relief (SR) treatment, reduced the hardness of the as-built alloy irrespective of aging times. At 200 °C, hardness decreases approximately linearly with aging time, indicating progressive over-aging. In contrast, at 250 °C, an initial hardness decrease is followed by a transient peak of (115 ± 1) HV10 at 250 °C/1.0 h, after which hardness decreases again in an approximately linear manner. Furthermore, the 300 °C/4.0 condition resulted in a lower hardness (75 ± 1 HV10) than that of the cast + T6, T6 ASTM, and T6 ISQ conditions. Similar results have been reported for the AB, DA, and T6 conditions [8,9,14,16]. These results indicate that the AlSi10Mg alloy produced by PBF-LB/M exhibits a narrow temperature–time window for achieving peak hardness with post-processing heat treatments.

### 3.2. XRD analysis

To investigate the structural features governing the aging behavior of the AlSi10Mg alloy manufactured by PBF-LB/M, four conditions were selected. The XRD patterns are presented in Fig. 3a for AB, DA 150/2.0, T6 ASTM, and T6 ISQ, and the corresponding structural parameters are summarized in Table 3.

The Al and Si diffraction peaks were confirmed using the Crystallographic Open Database patterns 9008460 [47] and 9011998 [48]. The indexed peak intensities in the XRD patterns correspond to the α-Al (Fm $\overline{3}$ m) and Si (Fd $\overline{3}$ m) phases and suggest weak crystallographic texture under all investigated conditions. The intensity of the Si phase peaks increases with DA 150/2.0 and intensifies after T6 ASTM and T6 ISQ. The presence of $Mg_2Si$ was not detected in the current study due to a mass fraction (~0.4 wt% of Mg) below the detection limit of the used XRD device. It is also noticed that Si remains in supersaturation in AB for which a Si phase fraction of (6.3 ± 0.1) wt.% was calculated from Rietveld refinement, whereas Si starts to precipitate from supersaturation after DA 150/2.0 treatment, leading to a higher Si phase fraction (7.7 ± 0.1 wt%), and reaches the nominal composition after the T6 ASTM (10.4 ± 0.1 wt%) and T6 ISQ (10.2 ± 0.1 wt%) treatments. These results are consistent with the calculated lattice parameters of the α-Al and Si phases plotted in Fig. 3b.

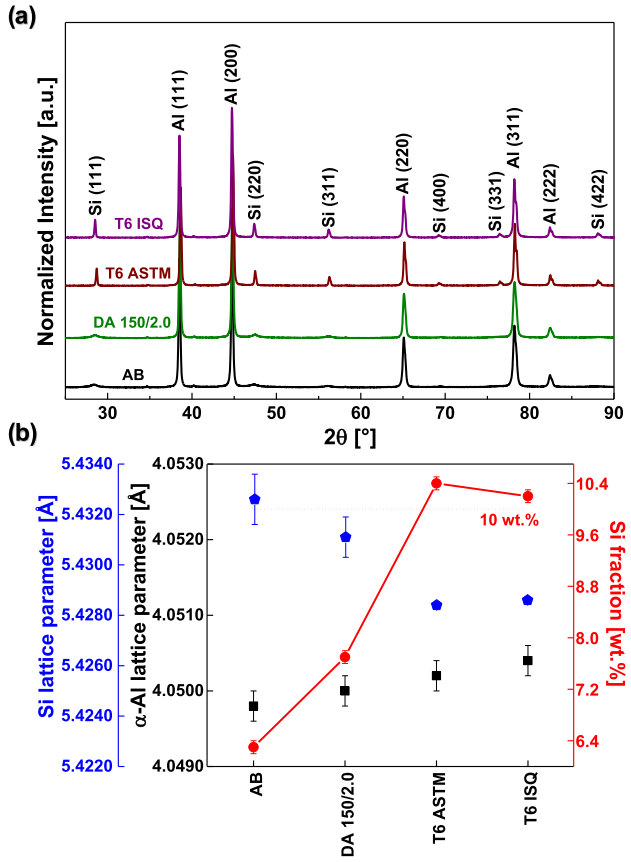


**Fig. 3.** (a) XRD patterns under different heat-treatment conditions and (b) lattice parameters of the α-Al and Si phases with the corresponding Si phase fraction.

**Table 3**
Structural parameters of the identified phases determined by Rietveld refinement of the XRD patterns.

| Parameter/Condition | AB | DA 150/2.0 | T6 ASTM | T6 ISQ |
|---|---|---|---|---|
| **Phase fraction, wt.%** | | | | |
| α-Al (Fm $\overline{3}$ m) | 93.7 (2) | 92.3 (2) | 89.6 (2) | 89.8 (2) |
| Si (Fd $\overline{3}$ m) | 6.3 (1) | 7.7 (1) | 10.4 (1) | 10.2 (1) |
| **Lattice parameter, Å** | | | | |
| a(Al) | 4.0498 (2) | 4.0500 (2) | 4.0502 (2) | 4.0504 (2) |
| a(Si) | 5.4326 (10) | 5.4311 (8) | 5.4284 (1) | 5.4286 (1) |
| **Microstrain, %** | | | | |
| Al (FWHM) | 0.174 (4) | 0.163 (5) | 0.156 (8) | 0.161 (11) |
| **Fit quality** | | | | |
| Rwp (%) | 7.3 | 7.7 | 9.8 | 8.5 |

A progressive increase in the α-Al phase lattice parameter was observed after heat treatment (Table 3 and Fig. 3b), varying from 4.0498 Å in the AB condition to 4.0504 Å after the T6 ISQ treatment, followed by a decrease in the Si lattice parameter from 5.4326 Å to 5.4286 Å, as a result of Si precipitation from supersaturation. A reduction in the microstrain of the α-Al phase was also observed, from 0.174% in the AB condition to 0.156% after the T6 ASTM treatment, suggesting that lattice distortion of the AB progressively recovered after the applied heat treatments.

### 3.3. Microstructural investigation

The microstructure of the as-built (AB) is shown in Fig. 4a, and direct aging at 150 °C for 2 h (DA 150/2.0) is shown in Fig. 4b. In addition, the microstructure of the sample treated at 300 °C for 4 h (DA 300/4.0) was investigated (Fig. 4c), as well as those obtained after solution (ST ASTM and ST ISQ) and T6 temper (T6 ASTM and T6 ISQ) (Fig. 5).

The laser tracks and their corresponding melt pools are revealed in the optical micrographs of the AB and DA 150/2.0 conditions. The contrast in the images clearly shows the semi-elliptical morphology of the melt pools as well as the microstructural heterogeneity at their boundaries, also known as heat-affected zones (HAZs), which are inherent to laser processing and the steep thermal gradients characteristic of alloys produced by PBF-LB/M.

The AB (Fig. 4a) and DA 150/2.0 (Fig. 4b) conditions exhibit similar mesostructures, indicating that the effects of DA 150/2.0 occur at a finer, micrometric scale. In contrast, partial homogenization is observed after DA 300/4.0 (Fig. 4c), with the melt pool boundaries becoming scarcely distinguishable. Following the solution treatment (Fig. 5a and c) and T6 tempers (Fig. 5b and d), the samples presented an isotropic microstructure with Si particles dispersed in the α-Al matrix.

The microstructures of the AB, DA 150/2.0 and DA 300/4.0 samples are also observed in the SEM images shown in Fig. 6. In the AB condition, the microstructure consists of a fine cellular Al matrix decorated by a continuous Si network at the cell boundaries (Fig. 6a1-a3) and a weak dispersion of very small Si particles within the cells (inset of Fig. 6a2).

In the DA 150/2.0 condition (Fig. 6b1-b3), significant Si precipitation is noticed within the α-Al cell, while the remaining eutectic Si at cell

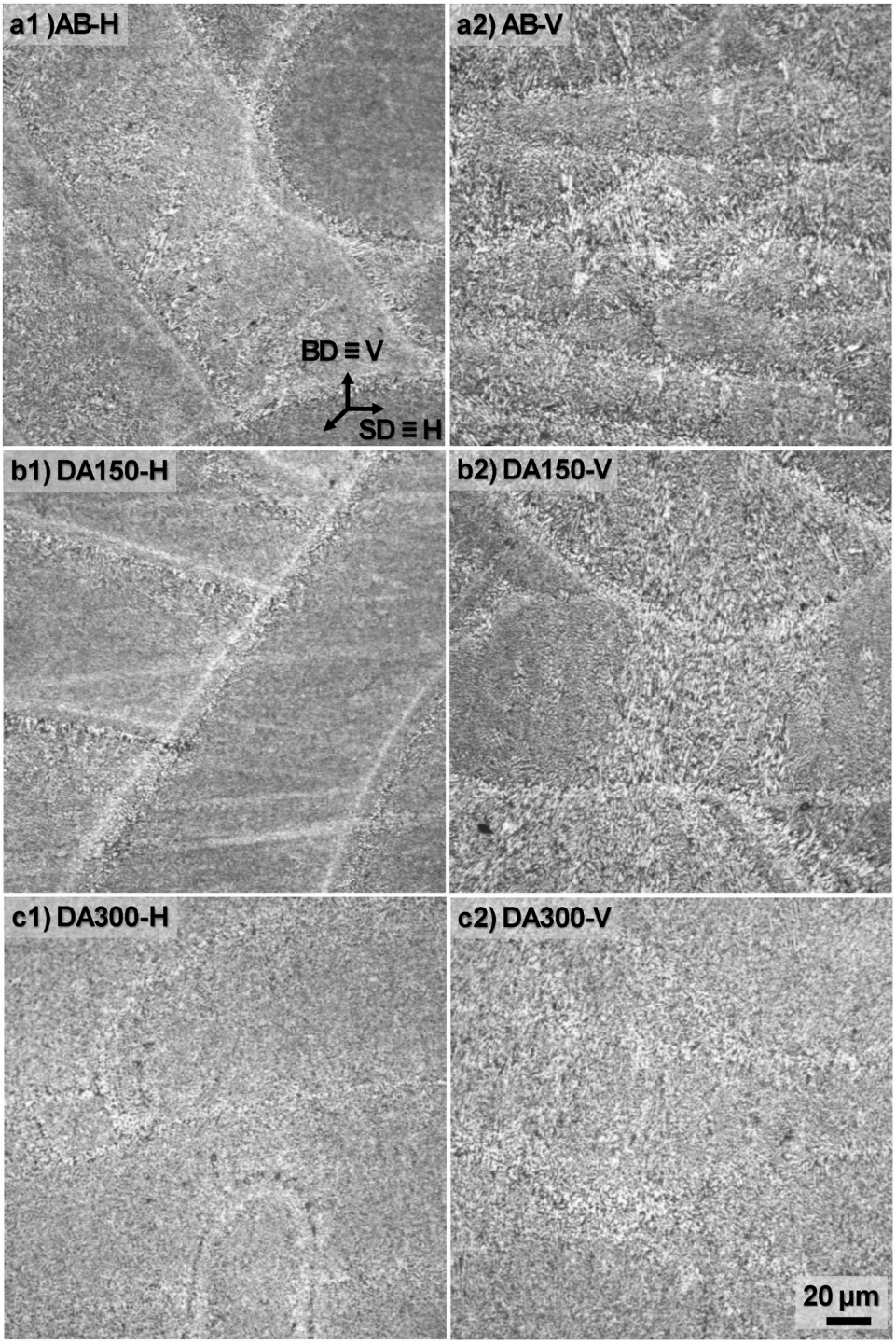


**Fig. 4.** Optical micrographs of the alloy in different conditions: (a1-a2) as-built, (b1-b2) DA 150/2.0, and (c1-c2), DA 300/4.0. H denotes the horizontal direction (parallel to the scanning direction, SD), and V denotes the vertical direction (parallel to the building direction, BD).

boundaries becomes noticeably thicker, and the network continuity decreases. After DA 300/4.0, the solidification substructure is dissolved (Fig. 6c1-c3). The Si network at the cell boundaries is no longer observed, and the microstructure is characterized by a uniform dispersion of Si particles within the α-Al matrix.

After solution (Fig. 7a and c) and T6 treatments (Fig. 7b and d), the eutectic Al–Si network was fully transformed into α-Al matrix containing coarsened Si particles, indicating that overaging occurred. T6 ISQ consistently exhibits smaller Si particles than T6 ASTM. Furthermore, β-AlFeSi is observed after solution and T6 treatments.

Fig. 8 shows the relationship between Si particle size and Vickers hardness for each condition. In the as-built (AB) condition, Si particles displayed equivalent diameters of 0.156–0.176 μm in the melt pool (MP) and slightly coarser (0.166–0.177 μm) in the heat-affected zone (HAZ). The horizontal sections typically present slightly coarser Si particle sizes. The Si-network area fraction was within 24%–28%, and the mean Si-network width was approximately 0.041–0.051 μm. This refined cellular microstructure with submicron Si network is associated with the high hardness and strength of as-built AlSi10Mg alloy produced by PBF-LB/M [8,9,12,14–16,33,49,50].

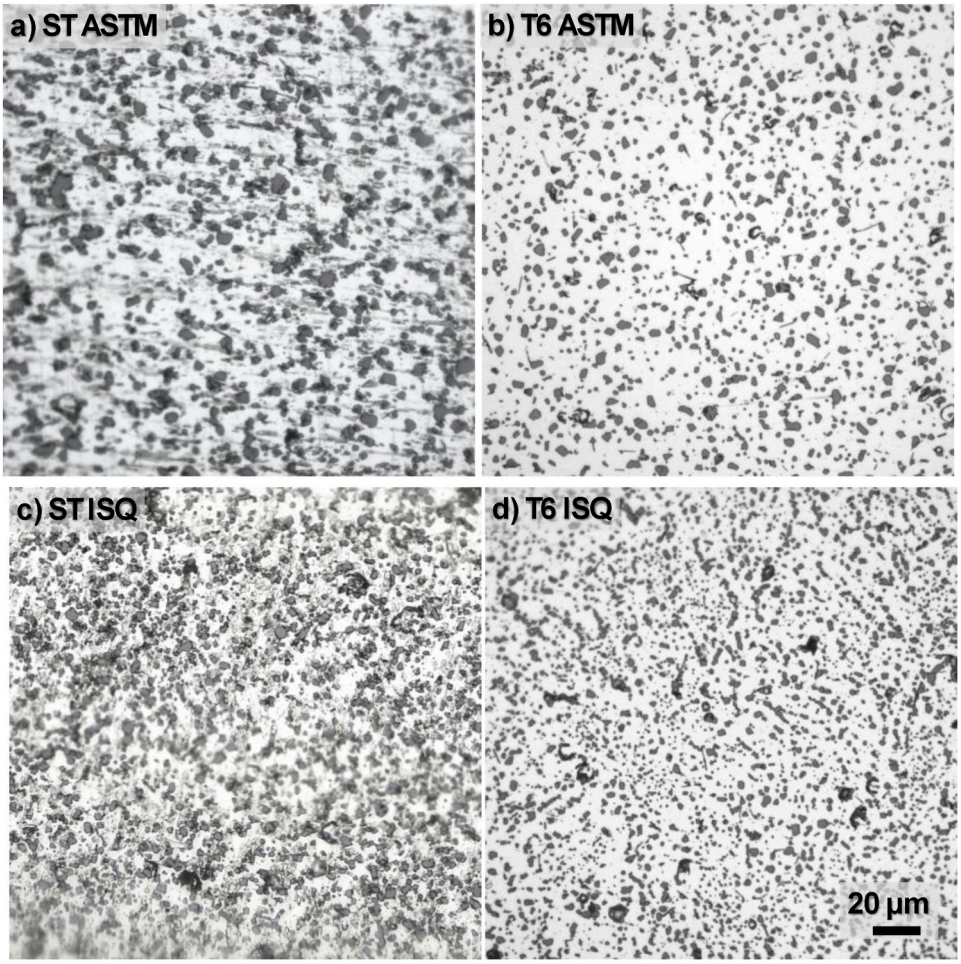


**Fig. 5.** Optical micrographs: (a) ST ASTM, (b) T6 ASTM, (c) ST ISQ, and (d) T6 ISQ.

After direct aging at 150 °C for 2 h (DA 150/2.0), the Si-network width slightly increased to 0.047–0.056 μm, while the Si-network area fraction varied between 28% and 34%. Moreover, a significant precipitation of Si within the α-Al cells occurred with an equivalent diameter of 0.166–0.170 μm in the MP and 0.170 μm in the HAZ. These microstructural features explain the peak hardness obtained after direct aging under those conditions. On the other hand, a higher aging temperature of 300 °C for 4 h (DA 300/4.0) led to a pronounced coarsening of the Si phase: Particle equivalent diameters ranged from 0.232 to 0.301 μm, almost twofold coarser than the AB condition, followed by a decrease in hardness.

In the ST ASTM and ST ISQ conditions, Si particles exhibited similar equivalent diameters of (2.1 ± 1.5) μm and (1.9 ± 1.4) μm, respectively, with the slightly smaller particle size in the ST ISQ condition reflecting the reduced solution treatment time. This refinement is carried over to the subsequent T6 ISQ condition, which exhibits finer Si particles ((1.6 ± 0.9) μm) compared to the T6 ASTM treatment ((2.2 ± 1.2) μm). The reduced heat-treatment duration limits Si particle growth, resulting in a finer microstructure and higher hardness in the T6 ISQ condition ((102 ± 2) HV10) compared to the T6 ASTM ((90 ± 1) HV10). This indicates that reducing the solution treatment time promoted increased precipitation during the subsequent aging step in the T6 ISQ treatment. Furthermore, the T6 treatments resulted in higher hardness than DA 300/4.0 and ST conditions, suggesting that β-AlFeSi and possibly $Mg_2Si$ precipitates contributed to the observed hardening. The large standard deviation in the average Si particle size indicates heterogeneity in the particle-size distribution.

### 3.4. Mechanical properties

The engineering tensile stress-strain curves of the heat-treated AlSi10Mg samples produced by PBF-LB/M are presented in Fig. 9, and the tensile properties are summarized in Table 4.

The as-built (AB) condition showed an elastic modulus (E) of approximately 74 GPa for both orientations. The yield strength ($\sigma_{YS}$) was (245 ± 4) MPa in the vertical direction (V) and (252 ± 8) MPa in the horizontal direction (H), while the ultimate tensile strength ($\sigma_{UTS}$) was (422 ± 14) MPa and (420 ± 17) MPa, respectively. The total elongation ($\varepsilon_T$) was about 4.6% in the vertical and 6.3% in the horizontal specimens. The relative density of the AB specimens was above 99.9% in both orientations. Therefore, while anisotropy is noticed in the total elongation, the AB specimens exceeded the tensile strength and ductility specified in the ASTM F3318-18a standard [35] in the vertical and horizontal directions.

For specimens directly aged at 150 °C for 2.0 h (DA 150/2.0), the tensile properties showed an increase in strength and ductility, together with reduced anisotropy: The total elongation was approximately 6.0% (V) and 7.0% (H), while the highest yield strength (286 ± 05 MPa and 285 ± 12 MPa for vertical and horizontal specimens) and ultimate tensile strength (474 ± 02 MPa and 442 ± 10 MPa, for vertical and horizontal orientations) were obtained. Relative densities remained above 99.9% for both directions. Therefore, DA 150/2.0 was identified as the optimal condition, as it maximized the hardness, strength and ductility of the alloy.

The solution-treated condition following the standardized route (ST ASTM) exhibited a decrease in the relative density to 98.4%,

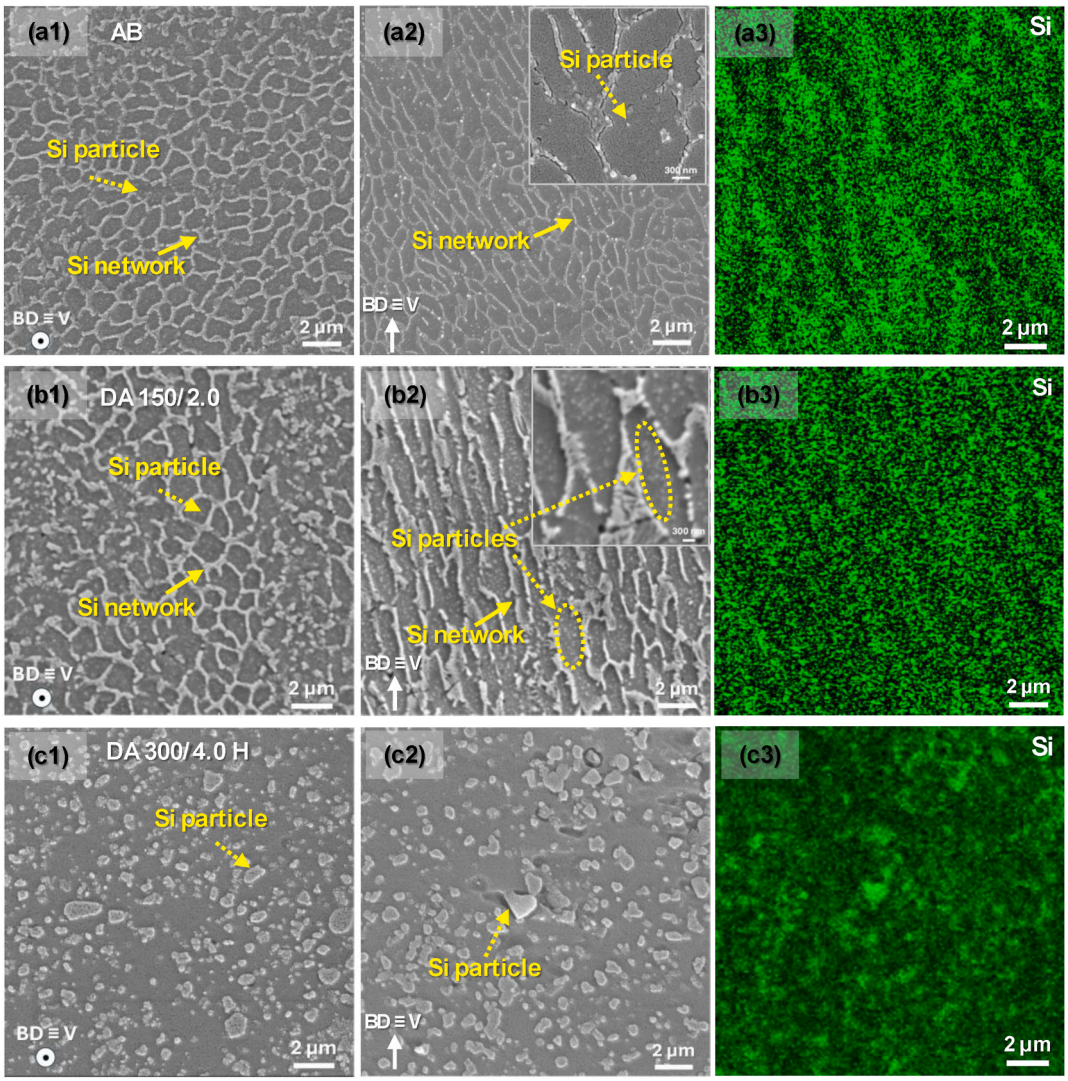


**Fig. 6.** Microstructure of the AlSi10Mg alloy under different conditions: (a1-a3) as-built, (b1-b3) DA 150/2.0, and (c1-c3) DA 300/4.0. Solid arrows indicate Si network along the Al cell boundaries, whereas dashed arrows denote Si particles dispersed within the cells. Corresponding EDS Si maps are shown in (a3), (b3), and (c3).

accompanied by a significant reduction in mechanical strength. The elastic modulus decreased to 46 GPa, with yield and ultimate tensile strengths of approximately 116 MPa and 166 MPa, respectively. The total elongation increased to 15.5%. In the specimens submitted to the standard full T6 heat treatment (T6 ASTM), the elastic modulus recovered to approximately 64 GPa. The yield strength was (226 ± 5) MPa (V) and (224 ± 26) MPa (H), while the ultimate tensile strength reached (266 ± 6) MPa and (250 ± 22) MPa. The total elongation decreased to (6.4 ± 0.7)% in the vertical and (8.8 ± 1.3)% in the horizontal directions compared to the ST condition, with relative densities near 99.0%. The ultimate tensile strength was below the specified (345 MPa) in the ASTM F3318-18a standard [35], but the ductility was significantly higher than the 5% of that standard. This underscores that conventional T6 was not strength-optimal for the AlSi10Mg alloy produced by PBF-LB/M.

The solution-treated according to the alternative schedule (ST ISQ) resulted in similar tensile strength to that of the ST ASTM condition, apart from a higher relative density (above 99.0%). The elastic modulus in this case was approximately 36 GPa, with a yield strength of (117 ± 4) MPa, ultimate tensile strength of (158 ± 2) MPa, and a total elongation of nearly 18.8%. The specimens submitted to the T6 ISQ treatment presented an elastic modulus of approximately 66 GPa. The yield strength reached (216 ± 21) MPa in the vertical and (183 ± 13) MPa in horizontal directions, and the ultimate tensile strength was (275 ± 20) MPa and (253 ± 11) MPa, respectively. Total elongation values were (7.7 ± 1.7)% for V and (8.0 ± 2.1)% for H directions. Therefore, the alternative T6 ISQ heat-treatment, although resulting in higher hardness, did not show a significant change in the tensile properties of the alloy compared to the standard T6 ASTM condition.

When assessing the strain-hardening capacity, estimated by the $\sigma_{UTS}/\sigma_{YS}$ ratio, a significant decrease is observed after T6 treatments, whereas the DA 150/2.0 condition maintains values comparable to the as-built state, indicating preserved work-hardening capability. This behavior contributes to the improved strength–ductility balance observed for the directly aged condition.

### 3.5. Fractography

Fig. 10 shows the fracture surfaces of the AlSi10Mg alloy in the AB and DA 150/2.0) conditions, as well as those obtained after solution (ST ASTM and ST ISQ) and T6 temper (T6 ASTM and T6 ISQ).

The fracture surface of the AB and DA 150/2.0 indicates a brittle fracture (Fig. 10a1-b2), with a clearly distinguishable morphology relative to the laser scan tracks characteristic of the PBF-LB/M process.

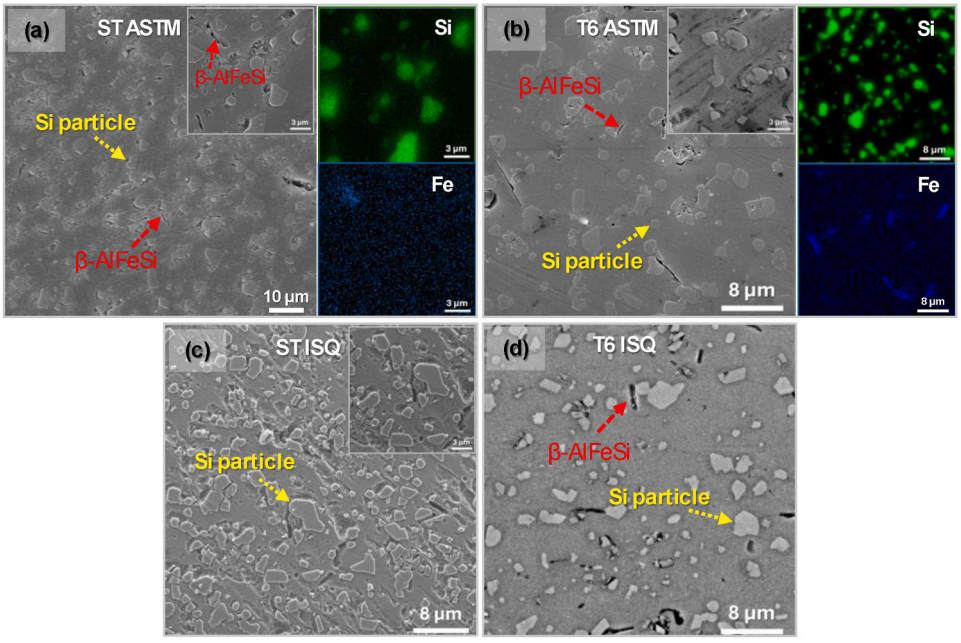


**Fig. 7.** Microstructure after (a) ST ASTM, (b) T6 ASTM, (c) ST ISQ, and (d) T6 ISQ. Images obtained with SE detector (a-c) and BSE detector (d).

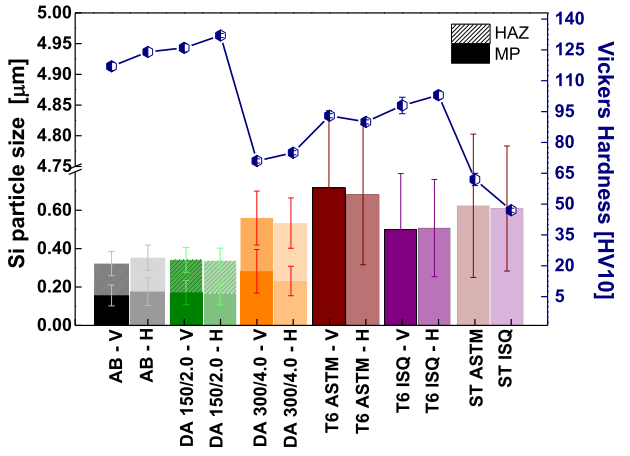


**Fig. 8.** Effect of Si particle size on Vickers hardness.

An anisotropic fracture behavior was observed in the AB condition: The fracture of vertical specimens (parallel to the building direction) happens in a plane parallel to the layers, leading to the inter-layer fracture observed in the inset of Fig. 10a2. On the other hand, horizontal specimens fractured through several layers, causing a *trans*-layer fracture (Fig. 10a1 and 11). As observed in the optical micrograph of AB horizontal tensile specimen (Fig. 11), a crack follows the laser-track overlap or heat-affected zones (HAZs), which are considered preferential paths for crack propagation [12,15,22,36,46].

The ST and T6 specimens showed characteristic ductile fracture surfaces (Fig. 10c–f). Moreover, fractured Si particles are often observed within the dimples of the T6 specimens (insets of Fig. 10d and f), whereas no decohesion of the Si particles from the matrix is observed. Pores were observed after ST and T6 treatments, indicating that these conditions led to the enlargement of gas pores.

## 4. Discussion

In this study, a comprehensive assessment of post-processing heat

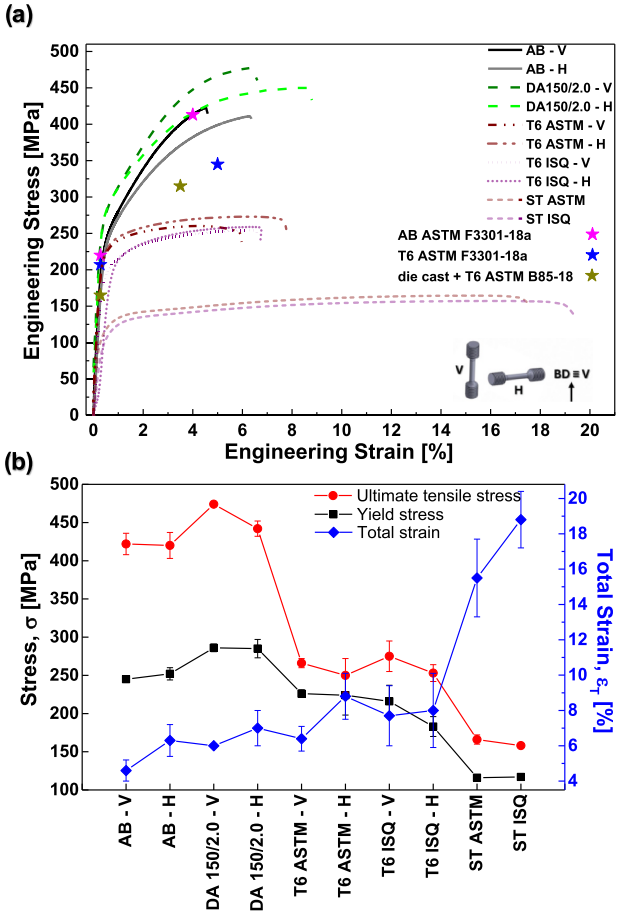


**Fig. 9.** (a) Engineering tensile stress-strain curves of representative specimens and (b) tensile properties.

treatments was conducted to establish the process–structure–property relationships governing the mechanical performance of heat-treated

**Table 4**
Tensile properties and relative density of the investigated conditions. V and H are the vertical and horizontal directions, respectively. E is the elastic modulus, $\sigma_{YS}$ the yield stress, $\sigma_{UTS}$ the ultimate tensile strength, and $\varepsilon_T$ the total elongation.

| Samples | E (GPa) | $\sigma_{YS}$ (MPa) | $\sigma_{UTS}$ (MPa) | $\sigma_{UTS}/\sigma_{YS}$ (−) | $\varepsilon_T$ (%) | Relative density (%) |
|---|---|---|---|---|---|---|
| AB - V | 74 ± 04 | 245 ± 04 | 422 ± 14 | 1.72 ± 0.07 | 4.6 ± 0.6 | 99.93 ± 0.02 |
| AB - H | 74 ± 10 | 252 ± 08 | 420 ± 17 | 1.67 ± 0.07 | 6.3 ± 0.9 | 99.96 ± 0.02 |
| DA 150/2.0 - V | 71 ± 03 | 286 ± 05 | 474 ± 02 | 1.66 ± 0.03 | 6.0 ± 0.1 | 99.97 ± 0.00 |
| DA 150/2.0 - H | 75 ± 07 | 285 ± 12 | 442 ± 10 | 1.56 ± 0.03 | 7.0 ± 1.0 | 99.91 ± 0.05 |
| ST ASTM | 46 ± 04 | 116 ± 04 | 166 ± 06 | 1.42 ± 0.08 | 15.5 ± 2.2 | 98.38 ± 0.70 |
| T6 ASTM - V | 64 ± 04 | 226 ± 05 | 266 ± 06 | 1.17 ± 0.01 | 6.4 ± 0.7 | 99.87 ± 0.05 |
| T6 ASTM - H | 72 ± 10 | 224 ± 26 | 250 ± 22 | 1.22 ± 0.09 | 8.8 ± 1.3 | 99.86 ± 0.11 |
| ST ISQ | 36 ± 06 | 117 ± 04 | 158 ± 02 | 1.37 ± 0.05 | 18.8 ± 1.6 | 99.06 ± 0.36 |
| T6 ISQ - V | 66 ± 06 | 216 ± 21 | 275 ± 20 | 1.26 ± 0.03 | 7.7 ± 1.7 | 99.83 ± 0.06 |
| T6 ISQ - H | 65 ± 10 | 183 ± 13 | 253 ± 11 | 1.44 ± 0.13 | 8.0 ± 2.1 | 99.88 ± 0.04 |
| AB (ASTM F3318-18a [35])[a] | - | 220 | 413 | 2.01 | 4 | - |
| T6 Temper (ASTM F3318-18a [35])[a] | - | 207 | 345 | 1.67 | 5 | - |
| die cast + T6 (ASTM B85-18 [46])[a] | - | 165 | 315 | 1.91 | 3.5 | - |

[a] minimum.

AlSi10Mg produced by PBF-LB/M. Particular emphasis is placed on correlating temperature–time conditions with microstructural evolution—namely Si precipitation, coarsening, and residual stress relaxation—and their effect on hardness and tensile behavior. Compared to previous studies, the present work adopts a more systematic experimental approach, exploring a wider range of temperature–time combinations to provide a clearer understanding of the mechanisms controlling hardening and ductility in PBF-LB/M AlSi10Mg. In addition, precipitation kinetics simulations are used to support the interpretation of the experimental trends, particularly the competition between precipitation and coarsening processes during aging.

Among the investigated temperature–time combinations, the highest hardness was obtained after direct aging (DA) at 150 °C for 2.0 h, without prior solution treatment (Fig. 2). Previous studies have similarly reported that DA at temperatures below 200 °C can effectively increase the hardness of AlSi10Mg produced by PBF-LB/M [19,29–32]. In addition, the hardening response during artificial aging is strongly influenced by natural aging. In this study, peak hardness was achieved only after at least 48 h of natural aging, followed by DA 150/2.0. This combination also resulted in a stable hardness level, as evidenced by the unchanged value after 144 h of natural aging. Extending the direct aging time at 150 °C beyond 2 h neither increased nor decreased the hardness, whereas increasing the aging temperature consistently led to lower hardness than that of the as-built (AB) condition. These findings are consistent with previous studies and highlight the importance of carefully coordinating additive manufacturing and post-processing heat treatments to achieve the specified desired strength levels for components in service [8,9,13,14].

A competitive hardening response was observed at intermediate temperatures normally used in stress-relief treatment [8,13,24], particularly between 200 °C and 250 °C, which can be rationalized by the competition between precipitation and coarsening kinetics. At 200 °C and 0.5 h, the hardness remains approximately the same as in the as-built state, similarly to other low-temperature aging treatments. With increasing time, however, the hardness decreases approximately linearly, indicating that coarsening becomes dominant. This is attributed to enhanced diffusion at this temperature, which promotes rapid growth and coarsening of existing precipitates, thereby reducing strengthening efficiency. In contrast, at 250 °C, the temperature is already high enough to promote both precipitation and coarsening from the early stages of aging. At 1.0 h, increased kinetic driving force accelerates the nucleation and growth of fine precipitates, resulting in a transient increase in hardness before coarsening mechanisms become dominant again. This interpretation is consistent with the work of Cauwenbergh et al. (2021), who performed DSC measurements on an as-built AlSi10Mg [8]. The authors identified two exothermic peaks on heating: the first, between 195 and 290 °C, attributed to Si precipitation, and the second, between 305 and 350 °C, associated with Si particle spheroidization due to increased diffusional activity [8]. Although their study was performed on PBF-LB/M AlSi10Mg alloy produced with a heated build plate at 200 °C [8], which is already high enough to induce precipitation, the results support the present findings, indicating that above 150 °C, coarsening and spheroidization of Si particles become significant, leading to hardness reduction. Moreover, increasing the aging temperature further reduced the hardness: Direct aging at 300 °C for 4 h led to lower values than those reported for the conventional die cast AlSi10Mg alloy. In addition, as widely reported [8,9,15,24,27–29], the T6 tempers did not harden the alloy produced by PBF-LB/M.

To quantitatively assess the influence of aging parameters on hardness, a two-way ANOVA was conducted considering aging temperature and time as independent factors. The analysis confirmed that both parameters significantly affect Vickers hardness ($p < 10^{-221}$ for temperature and $p < 10^{-36}$ for time), with temperature exhibiting a markedly stronger statistical influence. This result reinforces the experimentally observed dominance of temperature over time in governing the aging response.

This narrow temperature–time window was further examined using precipitation kinetics simulations. Therefore, in addition to the experimental investigation, a physically based modeling approach was employed to support the interpretation of the results. Unlike previous models reported in the literature, the present framework explicitly differentiates between as-built and solution-treated microstructures, enabling a direct comparison between direct aging and T6 conditions. Furthermore, it links precipitation kinetics with hardness, providing a physically consistent basis for interpreting the experimentally observed trends. Fig. 12 presents the predicted precipitation kinetics. The simulations confirm a strong precipitation tendency under the direct aging (DA) at 150 °C, previously identified as critical temperature for Si precipitation within the α-Al cells [51]. In contrast, the predicted volume fractions of clusters (GP zones), β”, and β’ remain comparatively small under the investigated conditions.

The calculated Si fractions (Fig. 11d) show good agreement with the experimental data (~8% wt.%), particularly with the XRD measurements for the direct aging at 150 °C for 2.0 h (DA 150/2.0) condition. Moreover, a trend is observed regarding the effect of using a reduced solution treatment and aging times in the ST ISQ and T6 ISQ conditions compared to their ASTM counterparts: shorter durations promote more

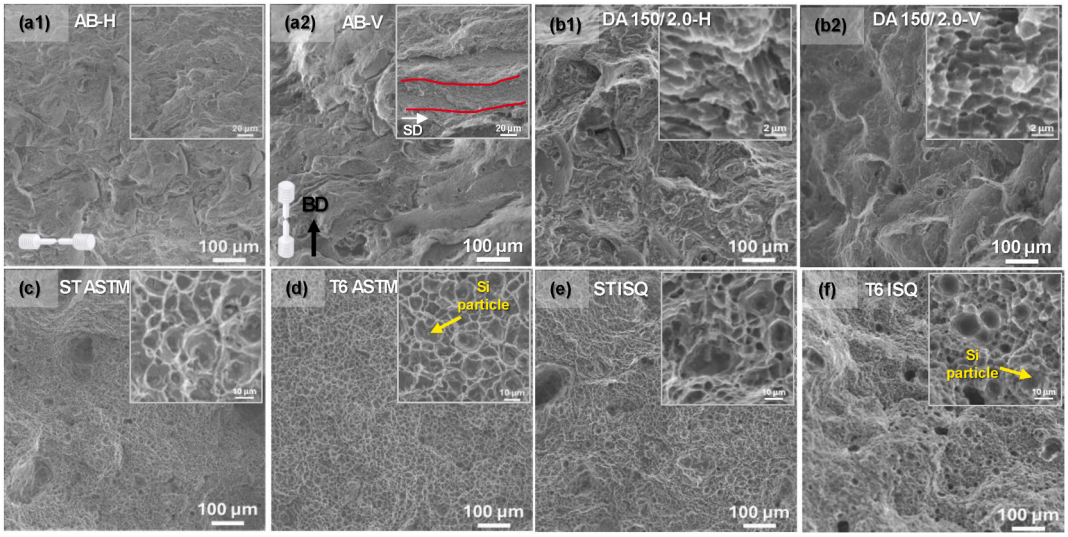


**Fig. 10.** Fracture surfaces of AB (a1–a2) and DA 150/2.0 (b1–b2) conditions, and fracture morphology after (c) ST ASTM, (d) T6 ASTM, (e) ST ISQ, and (f) T6 ISQ treatments.

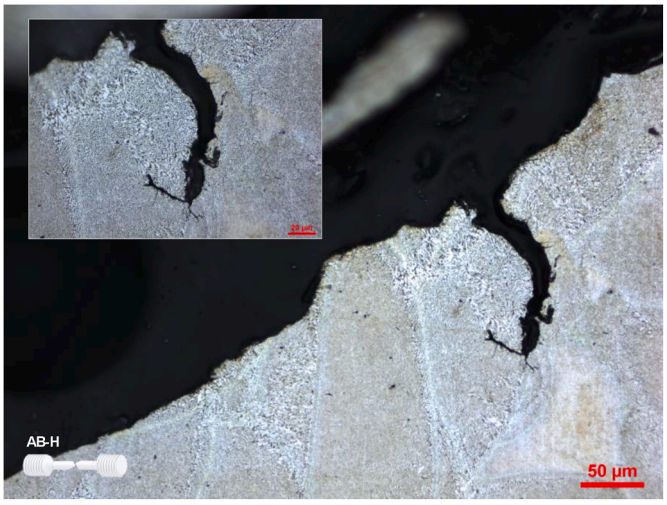


**Fig. 11.** Optical fractography of the as-built PBF-LB AlSi10Mg tensile specimen in the horizontal (H) direction.

precipitation. Nevertheless, the model predicts a continued evolution of precipitation with prolonged aging times, whereas the experimental results indicate a clear saturation of hardness. This discrepancy suggests that additional mechanisms—such as rapid solute exhaustion and early-stage precipitate coarsening—may limit further hardening during extended aging. Additional kinetic results, including predicted Si particle size and hardness evolution, are provided in the Supplementary Information (Supplementary Figure S2.5 and S2.6).

The X-ray diffraction (XRD) analyses (Fig. 3) and corresponding microstructural characterization (Figs. 4–7) provided insights into the obtained hardness trends. Based on the Al–Si phase diagram, the maximum solubility of Si in α-Al is approximately 1.6 wt% [11]. Hence, the XRD results suggest the non-equilibrium conditions in the AB samples, evidenced by the large amount of Si retained in α-Al solid solution, which is a direct consequence of the high cooling rates ($10^3$–$10^7$ K/s) associated with the PBF-LB/M process [16].

The lattice parameters of α-Al showed significant contraction in the as-built (AB), reflecting the high degree of Si supersaturation, in agreement with previous studies [11,16,18,24,25]. On the other hand, the progressive increase in the lattice parameter of the α-Al phase with heat treatment indicates relaxation of the supersaturated solid solution formed during PBF-LB/M, reflecting the redistribution of solute atoms within the Al matrix [16,24,25]. This agrees with the increase in the calculated Si mass fraction after DA 150/2.0, reaching the equilibrium mass fraction after the T6 treatments. As previously reported, residual Mg in solid solution may also contribute to the expansion of the α-Al lattice [51]. In addition, the gradual decrease in the Si lattice parameter with heat treatment indicates a relaxation of elastic strain as Si precipitated and coarsened, which drives the Si phase toward a stress-free lattice parameter characteristic of a fully relaxed crystal structure after the T6 treatments [16]. The progressive decrease in the microstrain of the α-Al phase from the AB condition to the T6 treatments further confirms the gradual release of lattice-distortion-induced stresses introduced during PBF-LB/M.

The microstructure of the as-built alloy revealed melt pools with α-Al cells surrounded by a continuous eutectic Al–Si network. This microstructure combined with a high dislocation density ($\sim 10^{14}$ $m^{-2}$) [20,52], the submicron size of the α-Al cells (Hall–Petch strengthening), and the supersaturated solid solution, accounts for the remarkable strength and strain-hardening of the as-built alloy. The microstructure after DA 150/2.0 remains similar to that of the AB condition, with eutectic Al–Si decorating the α-Al cells. However, DA 150/2.0 induces intensive precipitation of nanometric Si particles within the cells from the supersaturated α-Al matrix, which is responsible for the peak hardness observed after this treatment.

The melt pools and the eutectic Al–Si network are fully dissolved after DA 300/4.0, while coarse Si precipitates grow by Ostwald ripening. Similarly, samples submitted to solution (ST ASTM and ST ISQ) and T6 temper (T6 ASTM and T6 ISQ) present spheroidized Si particles (phase fraction of ~10 wt%) and acicular β-AlFeSi, suggesting that equilibrium conditions of the alloy were restored, leading to a significant hardness decrease. Although a slight difference is observed in the Si particle size between the standardized T6 ASTM and alternative T6 ISQ, neither of them hardened the alloy produced by PBF-LB/M.

Therefore, the (micro) structural characterization confirms that Si supersaturation in the α-Al phase of the as-built alloy is induced directly in PBF-LB/M processing of AlSi10Mg. In contrast, supersaturation in conventionally cast alloys is achieved only after a dedicated solution treatment followed by water quenching [16]. This confirms that artificial aging can be applied directly to the as-built condition of heat treatable alloys such as AlSi10Mg to induce precipitation of strengthening phases.

The refined microstructure, Al–Si eutectic network, supersaturated

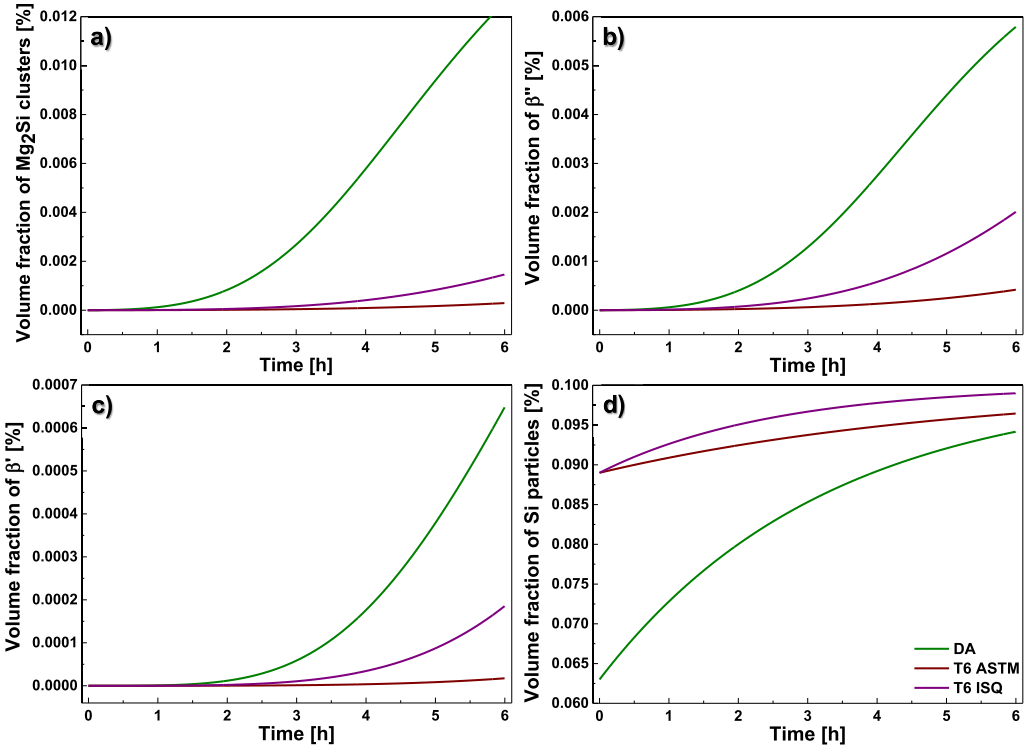


**Fig. 12.** Predicted evolution of precipitate volume fractions obtained from kinetic simulations.

solid solution, and high dislocation density resulting from the high cooling rates in PBF-LB/M are the main contributors to the high strength of AlSi10Mg in the as-built condition. In addition, there is widespread agreement in the literature that the Si-rich eutectic network surrounding the α-Al cells acts as a strong barrier to dislocation movements [12–20]. A significant strain hardening effect is observed for the AB and DA conditions, which exhibit a continuous Si-rich eutectic network.

As confirmed in the micrographs and XRD quantification, direct aging at 150 °C for 2.0 h preserves the Si network structure and induces intensive precipitation of nanometric Si particles with the Al matrix. Hence, the highest tensile strength is attained in the DA 150/2.0 condition (+17% yield strength and +12% ultimate tensile strength of the vertical specimens). The ductility of DA 150/2.0 was also increased compared with the AB alloy (+30% in the vertical direction). This improvement is associated with stress-relief and the reduced α-Al microstrain that results from Si precipitation out of solid solution. Previous studies have shown that nanometric Si particles in AlSi10Mg PBF-LB/M alloys are not cut by dislocations, acting as effective reinforcing obstacles through the Orowan mechanism [13,18,22,23,29,33,50–52]. These results confirm that the fine Si precipitates are primarily responsible for the improved mechanical properties of the heat-treated samples under the DA 150/2.0 condition.

The microstructure of the ST and T6 samples shows micrometric spheroidized Si particles dispersed within the softened α-Al matrix, which results in a significant strength loss (−8% YS and −59% UTS after T6 ASTM) and an increase (+39%) in ductility of vertical specimens relative to the as-built condition. The alternative T6 ISQ, performed with shorter solution and aging times, did not improve the tensile properties of the alloy compared to the standardized T6 ASTM, even though it resulted in slightly lower gas-induced porosity (0.14% compared to 0.17% under T6 ASTM). Moreover, the T6 treatments resulted in a significant reduction in the strain-hardening response of the alloy. Although AlSi10Mg can form $Mg_2Si$ during T6 treatments [11,15,16,19,51], it was not directly detected in any of the investigated samples in the current work. Nonetheless, the increase in tensile strength of the T6 samples compared to the ST conditions indicates that the T6-treated specimens may have been strengthened by $Mg_2Si$ particles, in addition to the observed β-AlFeSi phase.

The as-built (AB) and heat-treated conditions (DA, T6 ASTM and T6 ISQ) showed higher ductility in the horizontal compared to vertical specimens. On the other hand, no significant differences were observed in the elastic modulus (E), yield strength ($\sigma_{YS}$), or ultimate tensile strength ($\sigma_{UTS}$) results. Previous studies have reported a similar trend, which has been attributed to the orientation of the melt pools relative to the direction of the applied tensile loading [12,15,22,36,49]. It was also noticed an elastic modulus decrease after the high-temperature ST and T6 treatments. Similar results have been reported in previous studies [16,20,53,54], which are related to the (micro) structural modifications induced in the ST and T6 conditions, such as relaxation of the α-Al lattice due to Si precipitation out of supersaturation, with the additional contribution of pore coarsening after these treatments (Supplementary Figure S2.3).

The fracture surface of the AB and DA 150/2.0 generally indicate predominantly brittle fracture, with a morphology clearly associated with the laser scan tracks characteristic of the PBF-LB/M process, whereas the ST and T6 specimens showed ductile fracture surfaces. A pronounced anisotropic fracture behavior is observed especially in the AB condition, where fracture occurs along a plane parallel to the layers in the vertical specimens, resulting in distinct step-like features due to inter-layer failure (Fig. 10a2). On the other hand, horizontal specimens fractured through several layers, causing a more tortuous *trans*-track fracture propagation mechanism (Fig. 10a1). Moreover, a crack in an AB horizontal specimen could be observed nucleating in the Si network along melt pool boundaries (Fig. 11). This observation agrees with previous studies confirming that fracture in PBF-LB/M AlSi10Mg alloys frequently occurs preferentially along melt pool boundaries [12,15,22,36,46], also known as heat-affected zones (HAZs), resulting from hatch overlaps and by remelting-reheating of previous layers in PBF-LB/M. Furthermore, the HAZs are characterized by a coarser microstructure than within the melt pool (Fig. 8).

Since the DA 150/2.0 treatment does not significantly change the melt pool mesoscale structure of AlSi10Mg, the fracture mode remains similar to that of the as-built condition. Nevertheless, the fracture behavior becomes less anisotropic compared (Fig. 10b1-b2), and occurred at higher total elongations, showing more consistent crack propagation at approximately 45° to the loading direction. In addition to the expected relaxation of residual stress, a slight increase in microstructural uniformity contributes to this behavior. For vertical DA 150/2.0 specimens, higher-magnification views (insets of Fig. 10b2) reveal elongated shallow dimples, indicating limited but enhanced plastic deformation and reflecting the inclination of the fracture plane relative to the loading direction. This increased plasticity is associated with precipitation of nanometric Si particles within the α-Al cells (Fig. 6b1–b3) and partial dissolution of the Si network. Consequently, a moderate increase in ductility was observed in the DA 150/2.0 specimens, with higher total elongation values (Table 4), along with higher tensile properties, as the melt-pool boundaries become less dominant as crack-propagation paths.

The ST and T6 specimens exhibit ductile fracture characteristics, as evidenced by the presence of deeper and larger dimples (Fig. 10c–f). This behavior has been widely reported in the literature [12,36,46,55], indicating that heat treatments above 300 °C enhance ductility, although at the expense of mechanical strength, as reflected in Table 4 and Fig. 9. As observed in the micrographs (Figs. 5 and 7), the eutectic Al–Si network is completely dissolved, leading to the formation of an α-Al matrix containing coarsened Si particles. This results in a complete microstructural rearrangement, eliminating the characteristic HAZs arising from the PBF-LB/M process. Hence, fractured Si particles were often observed within dimples in the T6 treatments (insets of Fig. 10d and f), without decohesion of the Si particles from the matrix. In contrast, the fracture surfaces of the ST-treated specimens showed a lower density of Si particles within dimples. Furthermore, pores were observed after ST and T6 treatments, which can be attributed to the growth of pre-existing porosity during high-temperature exposure. However, the higher porosity in the ST and T6 specimens did not significantly affect ductility.

Although the as-built PBF-LB/M AlSi10Mg alloy exhibits high strength, its ductility is intrinsically limited by the fine cellular microstructure combined with a continuous eutectic Si network along cell boundaries. While this microstructural configuration is highly effective in strengthening the alloy, it promotes strain localization and early crack initiation, thereby restricting elongation at fracture. Consequently, the primary objective of post-processing heat treatments is to engineer the microstructure to overcome this ductility limitation without sacrificing strength, thereby achieving an improved strength–ductility balance.

The DA 150/2.0 condition emerges as the optimal treatment in this regard, delivering a simultaneous increase in strength and ductility. This response arises from the synergistic effects of residual stress relaxation, solute redistribution, and fine Si precipitation. The reduction of internal residual stresses lowers local stress concentrations, delaying crack initiation and promoting enhanced ductility. At the same time, the precipitation of fine Si particles from the supersaturated Al matrix strengthens the alloy while reducing microstrain, as evidenced by the evolution of the lattice parameters, microstrain values, and Si phase fractions obtained from XRD analysis. Importantly, this precipitation process occurs without extensive coarsening or disruption of the eutectic Si network, which remains largely preserved and continues to contribute to mechanical strength.

The results further demonstrate that the aging response of the AlSi10Mg produced by PBF-LB/M is governed by a narrow processing window. Aging at 150 °C promotes controlled precipitation and microstructural stabilization, whereas higher aging temperatures (200–300 °C) accelerate diffusion-driven coarsening, disrupt the Si network, promote the formation of coarse particles, and induce excessive stress relaxation. These effects are detrimental to the strength-ductility balance. The identification of this narrow temperature–time window therefore represents a key outcome of the present work and provides practical guidance for optimizing heat treatments of PBF-LB/M AlSi10Mg alloy.

## 5. Conclusion

The present work provides a systematic construction of aging curves for PBF-LB/M AlSi10Mg over a wide range of temperature–time conditions, complemented by a detailed correlational analysis of microstructural evolution, Si precipitation, and mechanical performance. Particular attention is given to evaluating whether a combination of high strength and improved ductility can be achieved directly through aging of the as-build condition, without the need for a prior solution treatment.

The results clearly demonstrate that AlSi10Mg produced by PBF-LB/M exhibits a narrow aging window in which significant strengthening can be achieved without a prior solution treatment. Direct aging at 150 °C for 2 h yielded peak hardness (133 ± 2 HV10) and the highest tensile performance, with increases of 17% in yield strength, 12% in ultimate tensile strength, and 30% in ductility in the vertical direction compared with the as-built condition.

These improvements result from the preservation of the eutectic Si network and the intensive precipitation of nanometric Si particles, which relieve microstrain in the α-Al matrix while maintaining the refined solidification structure intrinsic to PBF-LB/M. Conversely, higher aging temperatures (200–300 °C) and conventional T6 tempers promote rapid diffusion-driven coarsening, disrupt the Si network, and induce excessive stress relaxation, ultimately degrading the strength–ductility balance. Therefore, it was seen that the T6 and solution annealing treatments are appropriate for cast Al alloys, but they are not optimal for the fine microstructure of PBF-LB/M alloys.

Overall, the results demonstrate that direct aging can be effectively applied to the as-built condition of AlSi10Mg to induce strengthening while enhancing ductility, eliminating the need for a solution heat-treatment step. This approach provides a simplified, energy-efficient, and industrially relevant route for optimizing mechanical performance, offering a practical basis for the integration of PBF-LB/M into industrial post-processing and qualification frameworks.

## CRediT authorship contribution statement

**R.L. Batalha:** Conceptualization, Methodology, Investigation, Data curation, Formal analysis, Writing – original draft. **C.M. Ferreira:** Methodology, Data curation, Writing – review & editing. **A.C. Silva:** Methodology. **L. Reis:** Methodology, Writing – review & editing. **R. Cláudio:** Project administration, Funding acquisition, Validation, Writing – review & editing. **M.J. Carmezim:** Supervision, Writing – review & editing. **P. Ramasamy:** Data Curation, Writing – review & editing. **L.B. Godefroid:** Supervision, Writing – review & editing. **S.C. de Araújo:** Methodology. **G.L. de Faria:** Investigation, Formal analysis, Software, Writing – review & editing. **P.J. Morais:** Resources.

## Declaration of generative AI and AI-assisted technologies in the writing process

During the preparation of this work the authors used OpenAI ChatGPT-5 to improve the readability and language of the manuscript. After using it, the authors reviewed and edited the content as needed. The authors take full responsibility for the content of the publication.

## Declaration of competing interest

The authors declare that they have no known competing financial interests or personal relationships that could have appeared to influence the work reported in this paper.

## Acknowledgements

The authors acknowledge funding from the Agenda *Aero.Next Portugal* (2022-C05i0101-02 – Agendas/Alianças mobilizadoras para a reindustrialização), investment project N°. 31, financed by the Recovery and Resilience Plan (PRR) – Next Generation EU. Additional support was provided by Fundação para a Ciência e a Tecnologia (FCT) through IDMEC under LAETA (Project UID/50022/2025; https://doi.org/10.54499/UID/50022/2025). **R. L. Batalha** acknowledges funding from the base funding component of the Center for Technology and Innovation – ISQ, under the terms defined in AAC N°. 03/C05-i02/2022. **M. J. Carmezim** acknowledges financial support from the Centro de Química Estrutural (CQE) through the Fundação para a Ciência e a Tecnologia (FCT), under the project UID/00100/2025 (https://doi.org/10.54499/UID/00100/2025). **G. L. de Faria** acknowledges financial support from Brazilian National Council for Scientific and Technological Development (CNPq, Grant N°. 303908/2023-8).

## Appendix A. Supplementary data

Supplementary data to this article can be found online at https://doi.org/10.1016/j.jmrt.2026.03.256.

## Data availability

The dataset generated and analyzed in the study is included within this publication.

## References

[1] DebRoy T, Mukherjee T, Milewski JO, et al. Scientific, technological and economic issues in metal printing and their solutions. Nat Mater 2019;18:1026–32. https://doi.org/10.1038/s41563-019-0408-2.
[2] DebRoy T, Wei HL, Zuback JS, Mukherjee T, Elmer JW, Milewski JO, et al. Additive manufacturing of metallic components – process, structure and properties. Prog Mater Sci 2018;92:112–224. https://doi.org/10.1016/j.pmatsci.2017.10.001.
[3] Zhang J, Song B, Wei Q, Bourell D, Shi Y. A review of selective laser melting of aluminum alloys: processing, microstructure, property and developing trends. J Mater Sci Technol 2019;35(2):270–84. https://doi.org/10.1016/j.jmst.2018.09.004.
[4] Ruag Space. 3D printed satellite components. EOS GmbH customer success story. Available from: https://www.eos.info/industries/customer-success-stories/space/ruag-aerospace-3d-printed-satellite-components (accessed 15 February 2026).
[5] Metal Additive Manufacturing Magazine. Airbus satellite bracket production optimised by additive manufacturing. Available from: https://www.metal-am.com/airbus-satellite-bracket-production-optimised-by-additive-manufacturing/. [Accessed 15 February 2026].
[6] Saito S, Baba S, Kinoshita K, Takada N, Someya S. Thermal–hydraulic performance of additively manufactured crossflow minichannel heat exchangers. Appl Therm Eng 2025;274(A):126543. https://doi.org/10.1016/j.applthermaleng.2025.126543.
[7] Kusoglu IM, Gökce B, Barcikowski S. Research trends in laser powder bed fusion of Al alloys within the last decade. Addit Manuf 2020;36:101489. https://doi.org/10.1016/j.addma.2020.101489.
[8] Van Cauwenbergh P, Samaee V, Thijs L, et al. Unravelling the multi-scale structure–property relationship of laser powder bed fusion processed and heat-treated AlSi10Mg. Sci Rep 2021;11:6423. https://doi.org/10.1038/s41598-021-85047-2.
[9] Merino J, Ruvalcaba B, Varela J, Arrieta E, Murr LE, Wicker RB, et al. Multiple comparative heat treatment and aging schedules for controlling the microstructures and mechanical properties of laser powder bed fusion fabricated AlSi10Mg alloy. J Mater Res Technol 2021;13:669–85. https://doi.org/10.1016/j.jmrt.2021.04.062.
[10] Ren N, Li J, Zhang R, et al. Solute trapping and non-equilibrium microstructure during rapid solidification of additive manufacturing. Nat Commun 2023;14:7990. https://doi.org/10.1038/s41467-023-43563-x.
[11] Marola S, Manfredi D, Fiore G, Poletti MG, Lombardi M, Fino P, et al. A comparison of selective laser melting with bulk rapid solidification of AlSi10Mg alloy. J Alloys Compd 2018;742:271–9. https://doi.org/10.1016/j.jallcom.2018.01.309.
[12] Zhao L, Santos Macías JG, Ding L, Idrissi H, Simar A. Damage mechanisms in selective laser melted AlSi10Mg under as-built and different post-treatment conditions. Mater Sci Eng 2019;764:138210. https://doi.org/10.1016/j.msea.2019.138210.
[13] Cao Y, Lin X, Wang QZ, Shi SQ, Ma L, Kang N, et al. Microstructure evolution and mechanical properties at high temperature of selective laser melted AlSi10Mg. J Mater Sci Technol 2021;62:162–72. https://doi.org/10.1016/j.jmst.2020.04.066.
[14] Huang N, Luo Q, Bartles DL, Simpson TW, Beese AM. Effect of heat treatment on microstructure and mechanical properties of AlSi10Mg fabricated using laser powder bed fusion. Mater Sci Eng 2024;895:146228. https://doi.org/10.1016/j.msea.2024.146228.
[15] Girelli L, Tocci M, Gelfi M, Pola A. Study of heat treatment parameters for additively manufactured AlSi10Mg in comparison with corresponding cast alloy. Mater Sci Eng 2019;739:317–28. https://doi.org/10.1016/j.msea.2018.10.026.
[16] Fite J, Prameela SE, Slotwinski JA, Weihs TP. Evolution of the microstructure and mechanical properties of additively manufactured AlSi10Mg during room temperature holds and low temperature aging. Addit Manuf 2020;36:101429. https://doi.org/10.1016/j.addma.2020.101429.
[17] Jiang X, Xiong W, Wang L, Guo M, Ding Z. Heat treatment effects on microstructure–residual stress for selective laser melting AlSi10Mg. Mater Sci Technol 2020;36(2):168–80. https://doi.org/10.1080/02670836.2019.1685770.
[18] Ben Amir E, Grinberg E, Gale Y, Sadot O, Samuha S. Influences of platform heating and post-processing stress relief treatment on the mechanical properties and microstructure of selective-laser-melted AlSi10Mg alloys. Mater Sci Eng 2021;822:141612. https://doi.org/10.1016/j.msea.2021.141612.
[19] Di Egidio G, Tonelli L, Zanni M, Carosi D, Morri A, Ceschini L. Direct artificial aging of the PBF-LB AlSi10Mg alloy designed to enhance the trade-off between strength and residual stress relief. JAlloys Metallurgical Syst 2024;5:100063. https://doi.org/10.1016/j.jalmes.2024.100063.
[20] Zhang XX, Andrä H, Harjo S, Gong W, Kawasaki T, Lutz A, et al. Quantifying internal strains, stresses, and dislocation density in additively manufactured AlSi10Mg during loading–unloading–reloading deformation. Mater Des 2021;198:109339. https://doi.org/10.1016/j.matdes.2020.109339.
[21] Zhang H, Wang Y, Wang JJ, Ni DR, Wang D, Xiao BL, et al. Achieving superior mechanical properties of selective laser melted AlSi10Mg via direct aging treatment. J Mater Sci Technol 2022;108:226–35. https://doi.org/10.1016/j.jmst.2021.07.059.
[22] Delahaye J, Tchoufang Tchuindjang J, Lecomte-Beckers J, Rigo O, Habraken AM, Mertens A. Influence of Si precipitates on fracture mechanisms of AlSi10Mg parts processed by selective laser melting. Acta Mater 2019;175:160–70. https://doi.org/10.1016/j.actamat.2019.06.013.
[23] Fiocchi J, Tuissi A, Biffi CA. Heat treatment of aluminium alloys produced by laser powder bed fusion: a review. Mater Des 2021;204:109651. https://doi.org/10.1016/j.matdes.2021.109651.
[24] Katti I, Zhang D, Qiu D, Weiss M, Forsmark JH, Easton M. The effect of the isothermal heat treatment on the microstructure and properties of powder bed fusion–laser beam AlSi10Mg alloy. Adv Eng Mater 2024;26:2400202. https://doi.org/10.1002/adem.202400202.
[25] Phutela C, Bosio F, Li P, Aboulkhair NT. Correlating the microstructure and hardness of AlSi10Mg powder with additively manufactured parts upon in-situ heat treatments in laser beam powder bed fusion. Addit Manuf Lett 2023;7:100168. https://doi.org/10.1016/j.addlet.2023.100168.
[26] Casati R, Hamidi Nasab M, Coduri M, Tirelli V, Vedani M. Effects of platform preheating and thermal-treatment strategies on properties of AlSi10Mg alloy processed by selective laser melting. Metals 2018;8(11):954. https://doi.org/10.3390/met8110954.
[27] Kumar Ramavajjala A, Dandekar TR, Khatirkar RK, Joshi C, Chouhan RN, Agnihotri A. A review on the correlation between microstructure, heat treatment and mechanical properties of additively manufactured AlSi10Mg by LPBF. Crit Rev Solid State Mater Sci 2025;50(3):239–74. https://doi.org/10.1080/10408436.2024.2414012.
[28] Amith KV, Baloor SS, Polishetty A, Bolar G, Govindhan AN. Heat treatment and its effect on machining induced surface roughness of cast and additive manufactured AlSi10Mg. Sci Rep 2025;15:26433. https://doi.org/10.1038/s41598-025-10732-5.
[29] Park TH, Baek MS, Hyer H, Sohn Y, Lee KA. Effect of direct aging on the microstructure and tensile properties of AlSi10Mg alloy manufactured by selective laser melting process. Mater Char 2021;176:111113. https://doi.org/10.1016/j.matchar.2021.111113.
[30] Zhang Z, Zhao Z, Li X, et al. Effect of direct aging on corrosion behavior of AlSi10Mg alloy fabricated by laser powder bed fusion. Acta Metall Sin 2024;37:266–82. https://doi.org/10.1007/s40195-023-01628-2.
[31] Tang H, Gao C, Zhang Y, Zhang N, Lei C, Bi Y, et al. Effects of direct aging treatment on microstructure, mechanical properties and residual stress of selective laser melted AlSi10Mg alloy. J Mater Sci Technol 2023;139:198–209. https://doi.org/10.1016/j.jmst.2022.08.032.
[32] Steuer R, Milkereit B, Wenner S, Broer J, Huber F, Schaper M, et al. Direct natural and artificial aging of aluminum alloy AlSi10Mg after laser powder-bed fusion. Adv Eng Mater 2025;27:2501181. https://doi.org/10.1002/adem.202501181.
[33] Baek MS, Kreethi R, Park TH, Sohn Y, Lee KA. Influence of heat treatment on the high-cycle fatigue properties and fatigue damage mechanism of selective laser melted AlSi10Mg alloy. Mater Sci Eng 2021;819:141486. https://doi.org/10.1016/j.msea.2021.141486.
[34] Fernandes RF, Jesus JS, Branco R, Borrego LP, Costa JD, Ferreira JAM. Effect of low-temperature stress relieving heat treatments on fatigue behaviour and failure mechanisms of L-PBF AlSi10Mg aluminium alloy. Eng Fail Anal 2025;169:109210. https://doi.org/10.1016/j.engfailanal.2024.109210.
[35] ASTM F3301-18a. Standard specification for thermal post-processing metal parts made via powder bed fusion. ASTM International; 2018.
[36] Girelli L, Giovagnoli M, Tocci M, Pola A, Fortini A, Merlin M, et al. Evaluation of the impact behaviour of AlSi10Mg alloy produced using laser additive manufacturing. Mater Sci Eng 2019;748:38–51. https://doi.org/10.1016/j.msea.2019.01.078.

[37] Hutchinson CR. Modeling the kinetics of precipitation in aluminium alloys. In: Lumley R, editor. Fundamentals of aluminium metallurgy. Woodhead Publishing; 2011. p. 422–67. https://doi.org/10.1533/9780857090256.2.422.
[38] Hu Y, Curtin WA. Modeling peak-aged precipitate strengthening in Al–Mg–Si alloys. J Mech Phys Solid 2021;151:104378. https://doi.org/10.1016/j.jmps.2021.104378.
[39] Massardier V, Meyruey G, Perez M. Characterization and modelling of the precipitation sequence of an Al–Mg–Si alloy with silicon excess for the prediction of the mechanical properties during ageing. Mater Sci Forum 2018;941:1161–6. https://doi.org/10.4028/www.scientific.net/msf.941.1161.
[40] Zhang Y, Sills RB. Strengthening via orowan looping of misfitting plate-like precipitates. J Mech Phys Solid 2023;173:105234. https://doi.org/10.1016/j.jmps.2023.105234.
[41] Rietveld HM. A profile refinement method for nuclear and magnetic structures. J Appl Crystallogr 1969;2:65–71. https://doi.org/10.1107/S0021889869006558.
[42] Lutterotti L, Scardi P. Simultaneous structure and size–strain refinement by the rietveld method. J Appl Crystallogr 1990;23:246–52. https://doi.org/10.1107/S0021889890002382.
[43] Popa NC. The (hkl)-dependent line broadening in a rietveld analysis. J Appl Crystallogr 1998;31:176–80. https://doi.org/10.1107/S0021889897009795.
[44] ASTM E92-23. Standard test methods for Vickers hardness and Knoop hardness of metallic materials. ASTM International; 2023.
[45] ASTM E8/E8M-22. Standard test methods for tension testing of metallic materials. ASTM International; 2022.
[46] ASTM B85/B85M-18e1. Standard specification for aluminum-alloy die castings. ASTM International; 2018.
[47] Wyckoff RWG. Crystal structures. second ed.vol. 1. New York: Interscience Publishers; 1963. p. 7–83.
[48] Hom T, Kiszenick W, Post B. Accurate lattice constants from multiple reflection measurements II. Lattice constants of germanium, silicon and diamond at 25 °C. J Appl Crystallogr 1975;8:457–8.
[49] Rosenthal I, Shneck R, Stern A. Heat treatment effect on the mechanical properties and fracture mechanism in AlSi10Mg fabricated by additive manufacturing selective laser melting process. Mater Sci Eng 2018;729:310–22. https://doi.org/10.1016/j.msea.2018.05.074.
[50] Alghamdi F, Song X, Hadadzadeh A, Shalchi-Amirkhiz B, Mohammadi M, Haghshenas M. Post heat treatment of additive manufactured AlSi10Mg: on silicon morphology, texture and small-scale properties. Mater Sci Eng 2020;783:139296. https://doi.org/10.1016/j.msea.2020.139296.
[51] Maeshima T, Oh-ishi K, Kadoura H. Microstructural evolution and hardening phenomenon caused by aging of AlSi10Mg alloy by laser powder bed fusion. Heliyon 2024;10:e28006. https://doi.org/10.1016/j.heliyon.2024.e28006.
[52] Hadadzadeh A, Shalchi Amirkhiz B, Mohammadi M. Contribution of $Mg_2Si$ precipitates to the strength of direct metal laser sintered AlSi10Mg. Mater Sci Eng 2019;739:295–300. https://doi.org/10.1016/j.msea.2018.10.055.
[53] Doty HW, Hernandez-Sandoval J, Ammar HR, Songmene V, Samuel FH. Determination of Young's modulus in aluminum alloys: role of precipitates, dispersoids, and intermetallics. J Mater Res Technol 2025;37:3549–62. https://doi.org/10.1016/j.jmrt.2025.06.186.
[54] Maleki E, Bidar A, Rahmdel K, Shao S, Shamsaei N. Laser beam powder bed fused AlSi10Mg: an overview on the effect of post-processing on the microstructure and mechanical properties. Mater Des 2026;261:115336. https://doi.org/10.1016/j.matdes.2025.115336.
[55] Di Egidio G, Martini C, Börjesson J, Ghassemali E, Ceschini L, Morri A. Influence of microstructure on fracture mechanisms of the heat-treated AlSi10Mg alloy produced by laser-based powder bed fusion. Materials 2023;16(5):2006. https://doi.org/10.3390/ma16052006.